


Quantum-well states in fractured crystals of the heavy-fermion material CeCoIn₅Nicolas Gauthier^{1,2,*}, Jonathan A. Sobota¹, Makoto Hashimoto,³ Heike Pfau^{1,4}, Dong-Hui Lu³, Eric D. Bauer,⁵ Filip Ronning⁶, Patrick S. Kirchmann,¹ and Zhi-Xun Shen^{1,2}¹*Stanford Institute for Materials and Energy Sciences, SLAC National Accelerator Laboratory, Menlo Park, California 94025, USA*²*Geballe Laboratory for Advanced Materials, Departments of Applied Physics and Physics, Stanford University, Stanford, California 94305, USA*³*Stanford Synchrotron Radiation Lightsource, SLAC National Accelerator Laboratory, Menlo Park, California 94025, USA*⁴*Advanced Light Source, Lawrence Berkeley National Laboratory, Berkeley, California 94720, USA*⁵*MPA-CMMS, Los Alamos National Laboratory, Los Alamos, New Mexico 87545, USA*⁶*Institute for Materials Science, Los Alamos National Laboratory, Los Alamos, New Mexico 87545, USA* (Received 6 July 2020; revised 18 August 2020; accepted 19 August 2020; published 8 September 2020)

Quantum-well states appear in metallic thin films due to the confinement of the wave function by the film interfaces. Using angle-resolved photoemission spectroscopy, we unexpectedly observe quantum-well states in fractured single crystals of CeCoIn₅. We confirm that confinement occurs by showing that these states' binding energies are photon-energy independent and are well described with a phase accumulation model, commonly applied to quantum-well states in thin films. This indicates that atomically flat thin films can be formed by fracturing hard single crystals. For the two samples studied, our observations are explained by free-standing flakes with thicknesses of 206 and 101 Å. We extend our analysis to extract bulk properties of CeCoIn₅. Specifically, we obtain the dispersion of a three-dimensional band near the zone center along in-plane and out-of-plane momenta. We establish part of its Fermi surface, which corresponds to a hole pocket centered at Γ . We also reveal a change of its dispersion with temperature, a signature that may be caused by the Kondo hybridization.

DOI: [10.1103/PhysRevB.102.125111](https://doi.org/10.1103/PhysRevB.102.125111)**I. INTRODUCTION**

The quantum well is a simple introduction to quantum mechanics that demonstrates the quantization of confined states. Yet, this simple problem is directly relevant in important applications such as diode lasers and quantum dots. The discretization of the energy levels due to confinement occurs in a variety of systems in particle and condensed matter physics. For example, in one-dimensional spin chain systems, the interchain interactions generate a potential well that confines the magnetic domain walls [1]. In metals, the electronic states can be confined by interfaces, a subject that has been studied thoroughly using photoemission spectroscopy [2].

In metallic thin films, the electronic states dispersing perpendicular to the film plane are confined by the top and bottom interfaces. The resulting potential boundaries force the formation of quantized wave functions. The study of quantum-well states (QWSs) is a well-established and powerful technique that can provide accurate information about single-particle lifetimes and dispersions of three-dimensional bands [2]. The approach was initially applied to elemental metals, such as Cu [3] and Ag [4,5], and can be used to characterize properties such as electron-phonon coupling. Tuning the quantum-well states by varying the film thickness has also been shown to modify the superconducting temperature in Pb [6]. More

recent works used QWSs to get further insights on correlated oxides [7–9] and characterize topological states in Bi, Sb, and Bi₂Se₃ [10–12].

Here we report the observation of QWSs, signatures typically associated with thin films, via angle-resolved photoemission spectroscopy (ARPES) of fractured single crystals of CeCoIn₅. This result is surprising, as a well-defined confinement potential is required to form QWSs. We demonstrate in Sec. III B that the states' binding energies are photon-energy independent, as expected for photoemission from two-dimensional (2D) QWSs. In Sec. III C, we analyze the observed states using a phase accumulation model, typically employed in thin films. We first obtain the shape of the dispersion along the confined direction without any assumption. The film thickness and quantum numbers of the QWSs are then determined by calibrating our results to previous measurements [13]. The results in Secs. III B and III C confirm that the observed states are QWSs. In Secs. III D and III E, we exploit the QWS properties to extract bulk properties of CeCoIn₅.

The material studied, CeCoIn₅, is a prototypical heavy fermion with a superconducting state below $T_c = 2.3$ K [14]. Magnetic interactions, dependent on the degree of itineracy of the f electrons [15], have been proposed to mediate to formation of Cooper pairs in this material [14] similar to other heavy-fermion materials [16,17]. Theoretical calculations with itinerant f electrons indicate that the electronic structure of CeCoIn₅ is composed of three bands crossing the

*nicolas.gauthier@stanford.edu

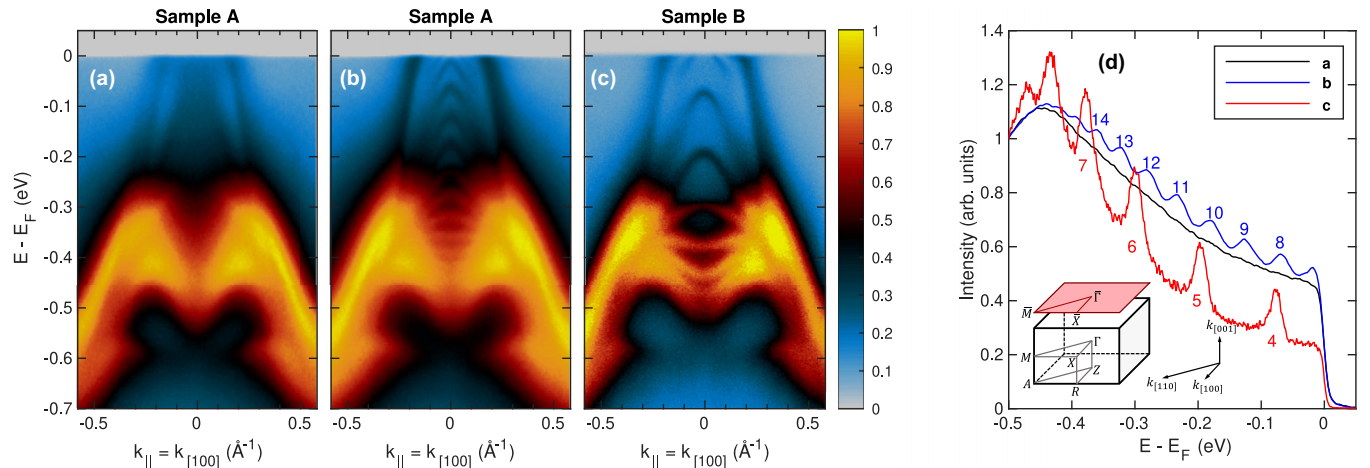


FIG. 1. Photoemission spectra measured with $h\nu = 25$ eV in p polarization along the $\bar{\Gamma}\bar{X}$ direction showing the presence of quantum-well states (QWSs). Spectra (a) and (b) have been measured on the same sample A but in different regions of its surface. Only the (b) spectrum reveals QWSs near $\bar{\Gamma}$. The spectrum (c) has been measured on sample B and exhibits a different number of QWSs, indicating a different quantization of the QWSs. (d) Energy distribution curves at $k_{\parallel} = 0$ from spectra (a) to (c). The quantum numbers n determined in Sec. III C are shown. Inset: Brillouin zone and its surface projection.

Fermi level E_F [18–20]. These have been investigated with quantum oscillations [18] and angle-resolved photoemission spectroscopy (ARPES) [13,21–27]. Most experimental observations of the Fermi surface are attributed to the nearly 2D α sheet and the quasi-2D β sheet. However, theory also predicts multiple three-dimensional (3D) sheets [18–20,28,29]. First, there is a 3D oblate pocket centered at Γ , which is labeled ϵ in Ref. [18] and γ in some ARPES works [13,27]. We will use the ϵ notation in this work. Second, there is also a 3D ellipsoidal pocket centered at X . Finally, there is a more complex 3D sheet around the ZRA plane, labeled γ_Z in Ref. [13]. A confinement potential along the c axis will mostly affect those 3D bands. Therefore, the QWSs observed in CeCoIn₅ must originate from one of these 3D bands. As explained in Sec. III D, our results indicate that the QWSs originate from the 3D ϵ pocket centered at Γ .

II. EXPERIMENTAL DETAILS

Large high quality samples of CeCoIn₅ were grown by flux as reported previously in Ref. [14]. The typical dimensions of the sample used in the experiment are $2 \times 2 \times 0.4$ mm³. Samples were fixed on a copper post with Silver Epoxy Epo-tek H20E and oriented to expose a (001) surface. A ceramic post was fixed on top of the sample surface with the same silver epoxy and samples were fractured *in situ* at temperatures below 20 K. We note that a large transverse force, of the order of a few Newtons, applied on the ceramic post was required to fracture the samples. ARPES measurements were performed at the beamlines 5-4 and 5-2 at Stanford Synchrotron Radiation Lightsource (SSRL). The chamber pressure remained below 4×10^{-11} Torr during the measurements. Measurements on sample A, and six other samples, were performed at the beamline 5-2 with a beam spot of 27×43 μm^2 . Linear horizontal (LH) polarized light with a photon energy of 25 eV was used. Complementary measurements were performed with photon energies ranging from $h\nu = 117$ to 127 eV. Measurements on sample B were

performed at the beamline 5-4 with a beam spot of 100×200 μm^2 . Measurements were acquired with circular right (CR), linear vertical (LV) and LH polarized light, for photon energies ranging from $h\nu = 7.5$ to 40 eV. Unless otherwise noted explicitly, measurements shown were taken with $h\nu = 25$ eV in LH polarization. For both beamline geometries, LV and LH polarizations correspond to s -polarized and p -polarized light, respectively.

III. EXPERIMENTAL RESULTS

A. Quantum well states in CeCoIn₅

A typical ARPES spectrum of CeCoIn₅ measured with 25 eV photons on sample A along the $\bar{\Gamma}\bar{X}$ direction is presented in Fig. 1(a). Based on the inner potential value of 12 eV [25], the perpendicular momentum k_{\perp} is at the Brillouin zone boundary. Therefore, this spectrum corresponds to a cut along the ZR direction and compares well with previous measurements along the same direction with 100 eV photons, also resulting in k_{\perp} near the Brillouin zone boundary [22]. The spectrum is characterized by an intense M-shaped feature between -0.6 and -0.3 eV, a sharp band extending from it to reach the Fermi level E_F , and a continuum filling the region between the M-shaped feature and the Fermi level near $k_{\parallel} = 0$. The observation of a continuum can be explained by a broadening of k_{\perp} due to final state effects [30]. It must then originate from a 3D band dispersing along the ΓZ direction.

The spectrum presented in Fig. 1(a) with its characteristic signatures has been consistently observed on many regions of sample A (see Appendix I) and on other samples. However, from the eight samples we measured, three of them exhibited different spectra in small regions of the surface. Examples of those uncommon spectra in samples A and B are shown in Figs. 1(b) and 1(c). In those spectra, numerous new bands appear near $k_{\parallel} = 0$ in the energy range between E_F and about -0.5 eV. We demonstrate in the following that these new bands in CeCoIn₅ are QWSs due to confinement along the c axis. We will show in Sec. III B that those states are

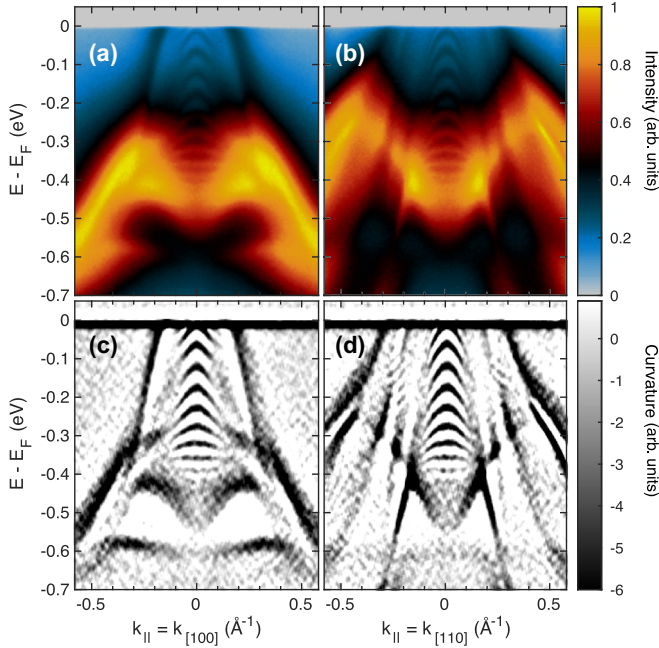


FIG. 2. Photoemission spectra along the $\bar{\Gamma}\bar{X}$ direction in (a) and the $\bar{\Gamma}\bar{M}$ direction in (b) measured on sample A. Measurements were taken using a photon energy of 25 eV in p polarization. Panels (c) and (d) present the 2D curvature plots associated to panels (a) and (b), respectively. The curvature plots highlight the QWSs near $\bar{\Gamma}$. Some hints of QWSs are also observed around $|k_{[110]}| = 0.25 \text{ \AA}^{-1}$ and $E - E_F = -0.15 \text{ eV}$ in (d).

photon-energy independent and in Sec. III C that they are well described by a phase accumulation model. In this model, the different number of bands between samples, as seen in Figs. 1(b) and 1(c), is understood from different thicknesses of the confinement region.

The spectrum in Fig. 1(b) is reproduced in Fig. 2(a) and the QWSs are made more apparent by presenting the 2D curvature of the photoemission intensity [31] in Fig. 2(c). Note that closely spaced levels only appear near $k_{||} = 0$ down to about -0.45 eV , in the same energy and momentum range where the continuum is observed in Fig. 1(a). A spectrum along $\bar{\Gamma}\bar{M}$, shown in Fig. 2(b), also exhibits the QWSs near $k_{||} = 0$. Its 2D curvature plot [Fig. 2(d)] also reveals less prominent QWSs around $k_{||} = k_{[110]} = \pm 0.25 \text{ \AA}^{-1}$ and -0.15 eV . Only wave vectors in the confined direction, i.e., along k_{\perp} , become quantized. In our geometry, this corresponds to the [001] direction while $k_{||}$ is aligned either along the [100] ($\bar{\Gamma}\bar{X}$) or [110] ($\bar{\Gamma}\bar{M}$) direction. The QWSs that are observed near $\bar{\Gamma}$ in Fig. 2 are associated with a 3D band dispersing along the ΓZ direction. This corresponds either to the 3D ϵ pocket centered at Γ or the concave γ_Z pocket centered at Z . On the other hand, the QWSs identified in Fig. 2(d), around $k_{[110]} = \pm 0.25 \text{ \AA}^{-1}$, most likely originates from the quasi-2D β sheet, which exhibits some dispersion along $k_{[001]}$.

B. Photon energy dependence

Due to their confinement along one direction, QWSs can be understood as 2D states that do not change their binding energy as a function of photon energy, in contrast to 3D

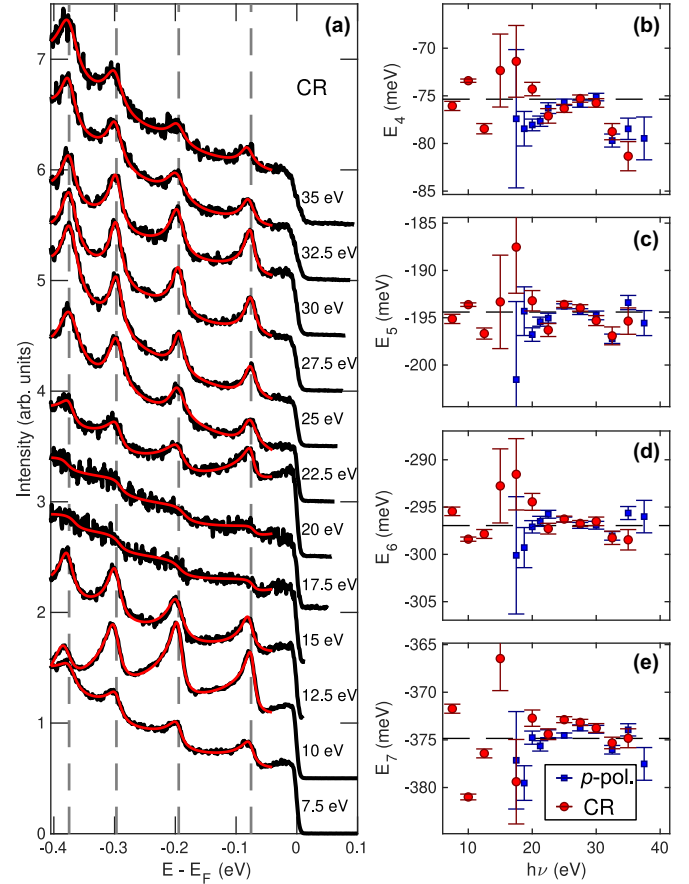


FIG. 3. Photon energy dependence of the QWSs on sample B. (a) EDCs at $k_{||} = 0$ using circularly polarized light from 7.5 to 35 eV. Red solid lines are a fit of four DS lineshapes to the data in black. Vertical gray dashed lines indicate the average energy of each QWS. (b)–(e) Peak positions of the four QWSs nearest to E_F obtained from the DS lineshape fit as a function of photon energy.

bulk bands [30]. The binding energies observed in CeCoIn_5 indeed are independent of the photon energy from 7.5 eV up to 37.5 eV, as shown in Fig. 3. The photon energy dependence reported here was performed on sample B with p -polarized and CR polarized light. The energy distribution curves (EDCs) measured at $k_{||} = 0$ are qualitatively similar for both polarizations and result in the same binding energy of the QWSs.

To extract the energies of the QWSs, the EDCs at $k_{||} = 0$ were fitted with

$$I = A(E) \sum_n f_{\text{DS}}(E - E_n, \Gamma_n, \alpha) + B(E), \quad (1)$$

where $f_{\text{DS}}(E - E_n, \Gamma_n, \alpha)$ is a Doniach-Šunjić (DS) lineshape [32] at energy E_n with a linewidth Γ_n and an asymmetry characterized by the parameter α , which is caused by the creation of electron-hole pairs. The functions $A(E)$ and $B(E)$ are quadratic polynomials accounting for the peak intensity variation and background, respectively. We fix the asymmetry parameter to be the same for all peaks of an EDC. The resulting fits are presented in Fig. 3(a) for the measurements performed with CR polarized light with photon energy from 7.5 eV up to 35 eV.

It is noteworthy that the position of the peak maximum of the DS lineshape $f_{\text{DS}}(E - E_n, \Gamma_n, \alpha)$ is different than the excitation energy E_n . They only coincide when either Γ_n or α tends toward zero. Experimentally, there are small shifts in the position of the peak maximum with photon energy but these can be related to a change of the asymmetry parameter α . The peak energies E_n extracted from the fit, presented in Figs. 3(b)–3(e), are effectively independent of the photon energy as expected for QWSs. In the following section, we use the binding energies averaged over all the photon energies to describe the QWSs of sample B at $k_{\parallel} = 0$. For sample A, a comparable photon energy dependence was not performed and the QWS binding energies at $k_{\parallel} = 0$ were instead determined from fitting its EDC in Fig. 1 with Eq. (1) using $\alpha = 0$.

C. Phase accumulation model

The binding energies of QWSs in thin films are defined by three important quantities: The film thickness d , the band dispersion of the bulk material in the direction perpendicular to the film plane $k_{\perp}(E)$, and the total phase shift $\Phi_{\text{total}}(E) = \Phi_{\text{top}}(E) + \Phi_{\text{bottom}}(E)$ occurring at the top and bottom boundaries of the confinement potential. This is expressed mathematically in a phase accumulation model by the Bohr-Sommerfeld quantization rule [2]:

$$2k_{\perp}(E)d + \Phi_{\text{total}}(E) = 2\pi n. \quad (2)$$

This equation establishes the conditions to obtain a standing wave in the film. Here, n is the quantum number of the QWS and the next state $n + 1$ is reached by adding one node in the standing wave. Typically, measurements are performed on many thin films with different known thicknesses [33]. These can be used together with Eq. (2) to determine the dispersion $k_{\perp}(E)$. Here, the nature and size of the confinement potential is *a priori* unknown. However, the existence of confined states constrains the characteristics of the interfaces. An interface of CeCoIn₅ with another metal would lead to a leakage of the electronic wave function into that metal, hindering the formation of QWSs. The top and bottom interfaces must therefore be formed with an insulating medium. The top interface can confidently be assigned to a CeCoIn₅-vacuum interface. For simplicity, we assume that the bottom interface is also a CeCoIn₅-vacuum interface. While metallic indium inclusions from excess flux can exist in CeCoIn₅ samples, no intergrowth of insulating material is expected. This further supports the assumption of a CeCoIn₅-vacuum interface at the bottom, as vacuum is the only insulating medium present. This assumption allows us to define the total phase shift $\Phi_{\text{total}}(E)$. The phase shift at a metal-vacuum interface is approximated by:

$$\Phi_{\text{metal-vacuum}}(E) = \pi \left(\sqrt{\frac{3.4}{E_V - E} - 1} \right), \quad (3)$$

where E_V is the vacuum level defined by $E_V = E_F + \phi_{\text{metal}}$ [34–36]. Here, ϕ_{metal} is the metal work function. We measured $\phi_{\text{CeCoIn}_5} = 3.9$ eV with the experimental setup and the method described in Ref. [37].

The total phase shift ranges from -0.13π at $E - E_F = 0$ eV to -0.22π at -0.4 eV. This change in the region of

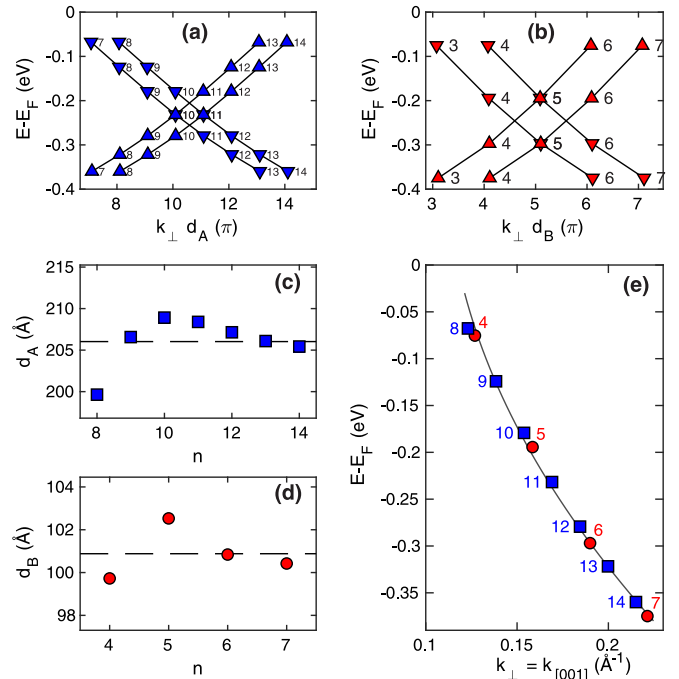


FIG. 4. (a) Dispersions for sample A, scaled by the thickness d_A , along the ΓZ direction for four different sets of quantum numbers. A negative (positive) band velocity is obtained for quantum numbers increasing (decreasing) with increasing binding energy. The total phase shift $\Phi_{\text{total}}(E)$ from the metal-vacuum interfaces is included but has a negligible effect on the dispersions. (b) Dispersions for sample B, presented as in panel (a). (c), (d) Calculated thickness d_A and d_B associated to each QWS for samples A and B, respectively, for the optimal sets of quantum numbers. The average thickness is indicated by the black dashed line. (e) Dispersion along the ΓZ direction based on the QWSs of samples A (blue squares) and B (red circle). The quantum number n of each QWS is indicated. The black line corresponds to the parametrized dispersion used to determine the thicknesses and quantum numbers.

interest is small in comparison to the 2π phase accumulated by each increment of the quantum number. Accordingly, the phase shift has a negligible contribution to the dispersion along k_{\perp} in Eq. (2). Furthermore, in the infinite box limit $\Phi_{\text{total}}(E) \rightarrow 0$, the shape of the dispersion is entirely given by the energy spacing between the QWSs. The thickness d and the quantum numbers n can only scale or shift the dispersion on the momentum axis. We illustrate this important point in Figs. 4(a) and 4(b). While we can safely assume that the observed states correspond to a consecutive sequence of quantum numbers, we do not know the offset value or whether this sequence is increasing or decreasing with energy. Using Eqs. (2) and (3), we evaluate the quantity $k_{\perp}d$ for the determined energies of the QWSs at $k_{\parallel} = 0$ using four different sets of quantum numbers. The quantity $k_{\perp}d$ corresponds to the dispersion scaled by the unknown film thickness. The lines in Figs. 4(a) and 4(b) connect the data points from one set of quantum numbers and provide a guide to the eye of this scaled dispersion. We observe that choosing increasing or decreasing quantum numbers as a function of binding energy changes the sign of the band velocity. The dispersion is shifted along the horizontal axis when the offset in the quantum number

series is varied. This shows that the shape of the dispersion is determined by the experimental results without any model parameters.

To pursue our analysis, we rely on data from literature to establish the sign and magnitude of the band velocity as well as its absolute momentum. Cleaving CeCoIn₅ to expose a (100) surface, Jang *et al.* measured the dispersion along [001] (Fig. S3b in Ref. [13]), corresponding to the dispersion along k_{\perp} at $k_{\parallel} = 0$ in our geometry. A well-defined hole band centered at Γ and a weaker diffuse hole band centered at Z are observed. The former agrees with the expectation of the ϵ oblate pocket centered at Γ from theory [19,38] and de Haas-van Alphen measurements [18]. For our analysis, we assume that the QWSs are associated with this hole band centered at Γ . Our choice is justified in Sec. III D. We parametrize the measured dispersion [13] between -0.38 eV and -0.03 eV by a second order polynomial $k_{\perp}(E) = aE^2 + bE + c$ with $a = 0.457$, $b = -0.108$, and $c = 0.118$.

Using this dispersion and Eq. (2), we evaluate the sample thickness for each QWS using a range of consecutive quantum numbers. The objective is to identify a set of quantum numbers for which the calculated thicknesses do not change from one QWS to the next. The set of quantum numbers that lead to the smallest standard deviation of the calculated thicknesses is chosen. The thickness variation for the selected sets of n for samples A and B are presented in Figs. 4(c) and 4(d). We obtain an average thickness of 206 Å, or 27.3 unit cells, for sample A and 101 Å, or 13.4 unit cells, for sample B. The obtained thicknesses are very sensitive to the parametrized dispersion and their absolute values should be taken with caution. Thickness values change by $\sim 3\%$ for a shift of the parametrized dispersion by 0.005 \AA^{-1} . Larger shifts or changes in the slope can also modify the optimal quantum numbers, leading to more significant changes in the thickness values. Using the average thickness values and the selected sets of quantum numbers, we present the dispersion along k_{\perp} obtained from the QWSs at $k_{\parallel} = 0$ in Fig. 4(e). The agreement with the parametrized dispersion, shown by the black solid line, confirms the validity of the approach.

D. 3D band structure and Fermi surface

Figure 5(a) illustrates the effect of confinement along k_{\perp} on a bulk band dispersing along k_{\parallel} and k_{\perp} . The confinement selects specific k_{\perp} values of the bulk band, as shown by the colored lines. These sections of the bulk dispersion, or QWSs, are projected on a 2D plane that is measured in thin films. Effectively, 2D spectra $I(E, k_{\parallel})$ of QWSs such as the ones in Figs. 2(a) and 2(b) provide the structure of a 3D object, i.e., the band energy as a function of two different momenta. Up to now, we applied the phase accumulation model only at $k_{\parallel} = 0$ to characterize the dispersion along the ΓZ direction, represented by the black dashed line in Fig. 5(a). In the following, we extract the complete surface $E(k_{\parallel}, k_{\perp})$ illustrated in gray. Specifically, we determine the band structure $E(k_{\parallel} = k_{[100]}, k_{\perp})$ and $E(k_{\parallel} = k_{[110]}, k_{\perp})$ from the spectra in Figs. 2(a) and 2(b). Those spectra are reproduced in Figs. 5(b) and 5(c), after a division by a Fermi-Dirac distribution convoluted with the energy resolution. The QWS positions, indicated by the circles, were determined by fitting EDCs to Eq. (1) with

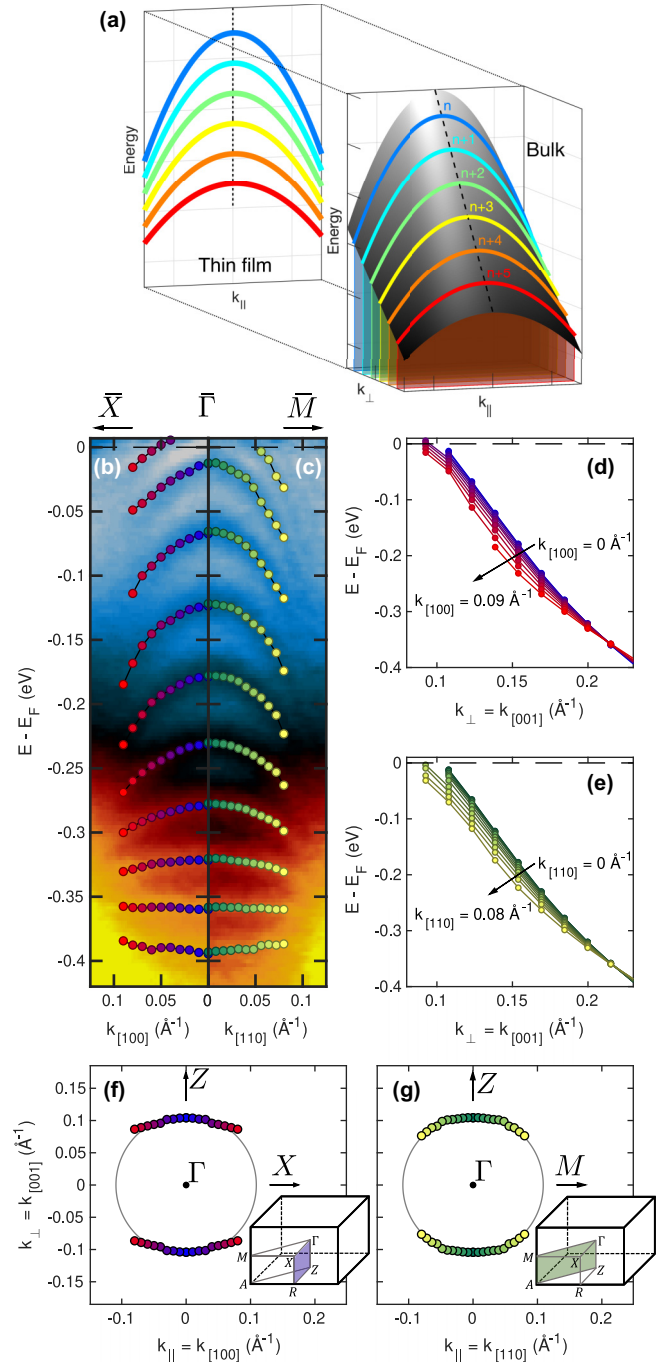


FIG. 5. (a) Representation of the effect of confinement on a bulk band dispersing along k_{\parallel} and k_{\perp} . Only sections of the bulk dispersion with specific k_{\perp} values are observed in thin films. (b), (c) Spectra along the $\Gamma\bar{X}$ and $\Gamma\bar{M}$ directions measured on sample A showing the QWSs and circles indicating their positions. The measurements were performed with $h\nu = 25$ eV in p polarization. (d), (e) Band dispersion along k_{\perp} for different values of k_{\parallel} . The momentum k_{\parallel} is along $\Gamma\bar{X}$ and $\Gamma\bar{M}$ in (d) and (e), respectively. (f), (g) Retrieved Fermi surface near Γ in the ΓZX and ΓZM planes, identified in the Brillouin zone. The circle centered at Γ is a guide to the eye.

$\alpha = 0$. Using Eq. (2) together with the determined quantum numbers and thickness, the dispersion along k_{\perp} at each values of $k_{\parallel} = k_{[100]}$ is calculated and shown in Fig. 5(d). These dispersions taken together form the surface $E(k_{\parallel} = k_{[100]}, k_{\perp})$.

The same data treatment is performed for values of $k_{\parallel} = k_{[110]}$ and is shown in Fig. 5(e).

With the established surfaces $E(k_{\parallel}, k_{\perp})$, we are able to determine sections of the Fermi surface associated with this band in two reciprocal lattice planes. For a fixed value of k_{\parallel} , the four data points of $E(k_{\parallel}, k_{\perp})$ closest to E_F are fitted to a second order polynomial. The perpendicular component of the Fermi momentum is determined by the intersection of this polynomial with E_F . The associated parallel component of the Fermi momentum corresponds to the fixed value of k_{\parallel} . This procedure is repeated at all values of k_{\parallel} and the Fermi momenta forming the Fermi surface are traced in Figs. 5(f) and 5(g) for the ΓZX and ΓZM planes, respectively. In both planes, the Fermi surface follows closely the arc of a sphere centered at Γ , although there is a small but visible anisotropy. As discussed in Sec. III C, we assigned the band forming the QWSs to the ϵ oblate hole pocket centered at Γ [18,19]. The theoretical calculations indicate that this pocket is slightly more extended along the ΓX direction than along the ΓM direction [19]. This is in agreement with the general tendency observed for the largest k_{\parallel} values in Figs. 5(f) and 5(g) and supports our analysis.

As indicated in Sec. III C, a hole band centered at Z is also observed in CeCoIn₅ [13] and it is associated to the γ_Z pocket. We performed the same analysis of Secs. III C and III D assuming that this band is responsible for the QWSs, instead of the ϵ pocket centered at Γ . This analysis results in a Fermi surface that is inconsistent with the theoretical results. It indicates the formation of an ellipsoidal pocket centered at Z while the theoretical calculations predict a concave pocket with the opposite curvature (see Fig. S2a in Ref. [13]). This disagreement by considering the γ_Z band and the agreement by considering the ϵ band justify the choice made in Sec. III C.

E. Temperature dependence

We characterize the temperature dependence of the QWSs for sample B using p -polarized light with 20 eV photons. By increasing temperature, there is a continuous shift of the QWS binding energy, as shown on Figs. 6(a)–6(d). However, the shift is more pronounced for the states closer to E_F . The temperature dependence of the QWSs suggests a change in the band structure, which can be caused by a change of the chemical potential as well as a modification of the band dispersion.

Note that each QWS has a fixed value of k_{\perp} which is enforced by Eq. (2) for a fixed quantum number n , assuming that the total phase shift $\Phi_{\text{total}}(E)$ is unchanged. This assumption is reasonable as $\Phi_{\text{total}}(E)$ does not change with temperature for vacuum-metal interfaces and its energy dependence is negligible. The only parameter that is allowed to change is the energy associated to a specific k_{\perp} value. A rigid band shift caused by a change of the chemical potential would therefore appear as an identical shift of all the QWSs. Experimentally, all the QWSs move towards E_F with increasing temperature, suggesting a change of the chemical potential, but their shift is not identical indicating the contribution from another effect. By reconstructing the k_{\perp} dispersion at $k_{\parallel} = 0$ at $T = 11$ K and 127 K, as shown in Fig. 6(e), we clearly observe a change in the dispersion, concurrently with

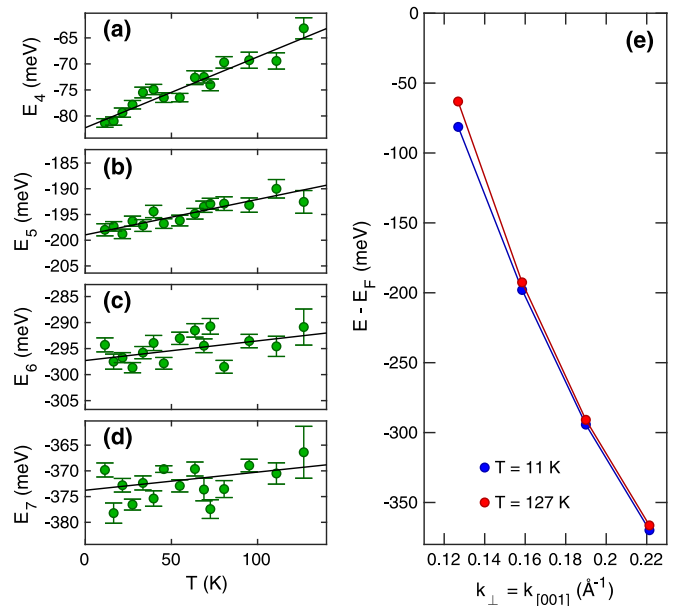


FIG. 6. Temperature dependence of the QWSs in sample B measured using 20 eV photons with p polarization. (a)–(d) Peak position of the QWSs as function of temperature obtained from fitting EDCs at $k_{\parallel} = 0$ to Eq. (1). The states nearest to E_F shift more than the others with temperature. (e) Dispersion along the ΓZ direction obtained from the QWSs at 11 and 127 K. There is small energy shift of the band and also a change in its slope near E_F .

a small chemical potential shift. This change in dispersion could be related to the formation of the heavy electronic liquid at low temperatures. Previous ARPES measurements on CeCoIn₅ [13,27] and YbRh₂Si₂ [39,40] have shown (i) that the Kondo hybridization decreases continuously as a function of increasing temperature and (ii) that the spectral signatures of the Kondo effect can be observed far above the Kondo coherence temperature, of 45 K in CeCoIn₅. A fading Kondo effect leads to a decrease of the hybridization gap between the renormalized f band and the conduction band. These changes occur close to E_F . In CeCoIn₅ one then expects the binding energy of the conduction band to decrease with increasing temperature close to E_F but be temperature-independent further away from E_F . This is consistent with our observation. The size of the hybridization gap was found to be linear in temperature up to 200 K for YbRh₂Si₂ [40], which is also consistent with our observation [Figs. 6(a)–6(d)].

IV. DISCUSSION

It is surprising that QWSs have not been reported previously in fractured CeCoIn₅ crystals, considering the numerous ARPES works present in the literature [13,21–27]. This is most likely because a specific set of conditions is required to observe them. In particular, a small beam spot was important to observe the QWSs in our experiments on CeCoIn₅. For example, we used a beam spot of $27 \times 43 \mu\text{m}^2$ at beamline 5-2 and QWSs were only observed in a small region of sample A (see Appendix I). Using a large beam spot or exploring only limited parts of the sample could prevent their observation.

The characteristics of the light also play a role in the observation of the QWSs. For example, the QWSs were not observed using *s*-polarized light (not shown). In *p* polarization, they were hardly visible at 15 eV and 17.5 eV. Previous works have been mostly performed at photon energies higher than 40 eV. In particular, ARPES measurements on CeCoIn₅ are often carried out in the vicinity of the Ce resonance at $h\nu = 121$ eV, in search of hybridization effects [13,21,24,26,27]. We also performed measurements on the QWSs for photon energies of 117 up to 127 eV in *p* polarization on sample A (see Appendix II). We observed that the photoemission cross section of the QWSs is strongly reduced at these larger photon energies and they only appear in a narrow energy range, from -0.45 eV to -0.2 eV. Thus, they can easily be overlooked and it could explain why QWSs were not reported earlier. We point out that the QWS photoemission intensity is unaffected by the Ce resonance at 121 eV. This is not surprising considering that *f*-spectral weight is not expected in the energy range where the QWSs are observed at this photon energy.

One of the most intriguing aspects of our results is the observation, in fractured single crystals, of spectroscopic signatures typically associated to thin films. This suggests that thin film-like structures are formed during the fracturing process. Our results indicate that we measure structures that are of comparable size to the beam spot ($27 \times 43 \mu\text{m}^2$ at beamline 5-2 and $100 \times 200 \mu\text{m}^2$ at beamline 5-4) and that are atomically flat in order to create well-confined QWSs. Previous STM results showed flat terraces of only tens of nanometers in CeCoIn₅ samples cleaved at room temperature [41]. Thin films grown by molecular beam epitaxy (MBE) also exhibit terraces significantly smaller than $1 \mu\text{m}$ [42]. In contrast, the observation of QWSs requires the presence of two parallel, atomically flat interfaces much larger than those seen in STM on cleaved crystals or MBE-grown films. The coexistence of different thicknesses in the regions probed in our samples is excluded as a single set of QWSs is observed. The coexistence of two thicknesses different by only one unit cell would exhibit QWSs separated by energies similar or larger than the experimental full width at half maximum.

The fracturing of our CeCoIn₅ crystals was performed at low temperatures ($T \approx 20$ K) by applying a large lateral force on a ceramic post glued to the sample surface. We note that fracturing our samples was rather difficult and required multiple attempts, due to the material hardness, the 3D nature of its structure and the large surface-area-to-thickness ratio of the samples. The unsuccessful attempts could have created cracks, easing the formation of flakes during fracturing. The high load applied is also more likely to induce branching effects known to occur in dynamic fractures [43]. In that case, a single crack dynamically splits in two cracks, which are expected to follow crystal planes [44]. Such a process could create free-standing thin flakes with parallel atomically flat surfaces. Assuming that such flakes are supported on their edges, vacuum on both sides of the flakes will prevent leakage of the electronic wave functions, leading to confinement. This interpretation suggests that the creation of thin films supporting QWSs might occur more generally in hard crystals when fracturing occurs under high mechanical load.

The physics of dynamical fractures in materials is rather complex but relevant for their mechanical properties. However, fracturing and its possible consequences are generally not addressed in strongly correlated systems such as CeCoIn₅. Recently, the effect of fracturing was also considered in the correlated material URu₂Si₂. In this case, it was shown that a one-dimensional charge density wave can be induced by fracturing at low temperatures [45]. This result, together with our observations, highlights that crystal fracturing can reveal unexpected phenomena in strongly correlated systems.

V. CONCLUSIONS

In summary, we reported the observation of spectroscopic signatures associated to QWSs in fractured single crystals of CeCoIn₅. We confirmed that those signatures are photon-energy independent and are described by a phase accumulation model, as expected for 2D QWSs. The dispersion of the 3D ϵ hole band along in-plane and out-of-plane momenta was obtained from a detailed analysis of the QWS spectra. From this result, sections of the Fermi surface were extracted and they are in agreement with theory. Finally, a temperature dependence of the QWSs revealed a change of the 3D dispersion that is consistent with a reduction of the Kondo hybridization with increasing temperature.

The observation of QWSs in a fractured single crystal is perhaps the most surprising result of our work. Indeed, a well-defined confinement potential is required to form sharp QWSs. Therefore, our work suggests that fracturing hard crystals at low temperatures can create large atomically flat thin film structures. This interesting observation is however not practical to do a systematic study of QWSs in CeCoIn₅. Further work with thin films obtained with controlled growth, which are available for CeCoIn₅ and related materials [42,46–48], would be of interest for a deeper investigation on how the Kondo hybridization is affecting the ϵ band.

The data from this study are available at the Stanford Digital Repository [49].

ACKNOWLEDGMENTS

This work was supported by the U.S. Department of Energy, Office of Basic Energy Sciences. N.G. acknowledges support from the Swiss National Science Foundation (fellowship no. P2EZP2 178542). H.P. acknowledges support from the German Science Foundation (DFG) under reference PF 947/1-1 and from the Advanced Light Source funded through U.S. Department of Energy, Office of Science. The Stanford Synchrotron Radiation Lightsource, SLAC National Accelerator Laboratory, is supported by the U.S. Department of Energy, Office of Science, Office of Basic Energy Sciences. Work at Los Alamos was performed under the auspices of the U.S. DOE, Basic Energy Sciences, Division of Materials Sciences and Engineering. N.G. is thankful to D.G. Mazzone for fruitful discussions.

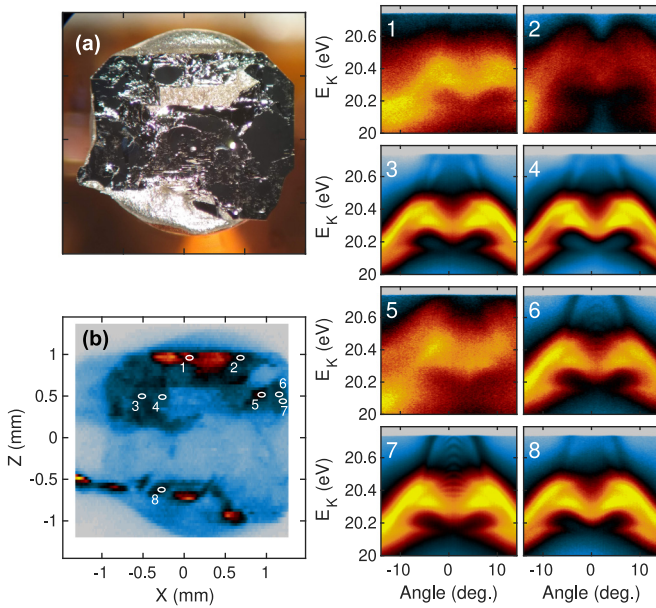


FIG. 7. (a) Picture of the sample A after fracturing. (b) Photoemission intensity map of the sample A. The intensity was integrated over the full angular range ($\pm 15^\circ$) and $20.51 \text{ eV} < E_K < 20.86 \text{ eV}$. White ellipses show different measurements positions (1 to 8). The size of the ellipse represents the beam spot size. On the right, spectra collected at the eight measurement positions are presented. Measurements were performed with 25 eV photon with p polarization, along the $\bar{\Gamma}\bar{X}$ direction.

APPENDIX A

Spectra obtained at different regions of the sample A are presented in Fig. 7. Regions 1, 2, and 5 have diffuse spectra, while sharp bands are observed in regions 3, 4, 6, 7, and 8. From these spectra, only regions 6 and 7 exhibit QWSs. Regions 3, 4, and 8 instead have diffuse intensity near $\bar{\Gamma}$.

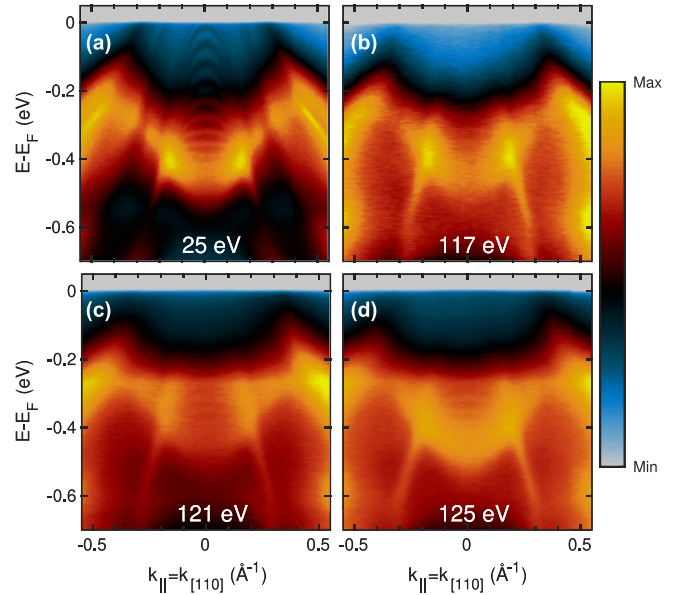


FIG. 8. (a)–(d) Photoemission spectra along the $\bar{\Gamma}\bar{M}$ direction measured on sample A with photon energies of 25, 117, 121, and 125 eV using p polarization.

APPENDIX B

In the main text, the measurements of QWSs for photon energies below 40 eV are reported. Here, we present measurements at photon energies around the Ce resonance of 121 eV on sample A along the $\bar{\Gamma}\bar{M}$ direction. The QWSs are also observed in this energy range, as shown in Figs. 8(b)–8(d). The contrast between the QWSs and the background is however strongly reduced, in comparison to the spectrum measured at 25 eV [Fig. 8(a)].

- [1] R. Coldea, D. A. Tennant, E. M. Wheeler, E. Wawrzynska, D. Prabhakaran, M. Telling, K. Habicht, P. Smeibidl, and K. Kiefer, Quantum criticality in an Ising chain: experimental evidence for emergent E_8 symmetry, *Science* **327**, 177 (2010).
- [2] T. C. Chiang, Photoemission studies of quantum well states in thin films, *Surf. Sci. Rep.* **39**, 181 (2000).
- [3] R. K. Kawakami, E. Rotenberg, H. J. Choi, E. J. Escorcia-Aparicio, M. O. Bowen, J. H. Wolfe, E. Arenholz, Z. D. Zhang, N. V. Smith, and Z. Q. Qiu, Quantum-well states in copper thin films, *Nature (London)* **398**, 132 (1999).
- [4] J. J. Paggel, T. Miller, and T. C. Chiang, Quantum-well states as Fabry-Perot modes in a thin-film electron interferometer, *Science* **283**, 1709 (1999).
- [5] J. J. Paggel, T. Miller, and T. C. Chiang, Temperature Dependent Complex Band Structure and Electron-Phonon Coupling in Ag, *Phys. Rev. Lett.* **83**, 1415 (1999).
- [6] Y. Guo, Y. F. Zhang, X. Y. Bao, T. Z. Han, Z. Tang, L. X. Zhang, W. G. Zhu, E. G. Wang, Q. Niu, Z. Q. Qiu, J. F. Jia, Z. X. Zhao, and Q. K. Xue, Superconductivity modulated by quantum size effects, *Science* **306**, 1915 (2004).
- [7] K. Yoshimatsu, K. Horiba, H. Kumigashira, T. Yoshida, A. Fujimori, and M. Oshima, Metallic Quantum Well States in Artificial Structures of Strongly Correlated Oxide, *Science* **333**, 319 (2011).
- [8] A. F. Santander-Syro, O. Copie, T. Kondo, F. Fortuna, S. Pailh s, R. Weht, X. G. Qiu, F. Bertran, A. Nicolaou, A. Taleb-Ibrahimi, P. Le F vre, G. Herranz, M. Bibes, N. Reyren, Y. Apertet, P. Lecoeur, A. Barth l my, and M. J. Rozenberg, Two-dimensional electron gas with universal subbands at the surface of SrTiO₃, *Nature (London)* **469**, 189 (2011).
- [9] W. Meevasana, P. D. King, R. H. He, S. K. Mo, M. Hashimoto, A. Tamai, P. Songsiririthigul, F. Baumberger, and Z. X. Shen, Creation and control of a two-dimensional electron liquid at the bare SrTiO₃ surface, *Nat. Mater.* **10**, 114 (2011).
- [10] P. F. Zhang, Z. Liu, W. Duan, F. Liu, and J. Wu, Topological and electronic transitions in a Sb(111) nanofilm: The interplay between quantum confinement and surface effect, *Phys. Rev. B* **85**, 201410(R) (2012).
- [11] S. Ito, B. Feng, M. Arita, A. Takayama, R.-Y. Liu, T. Someya, W.-C. Chen, T. Iimori, H. Namatame, M. Taniguchi, C.-M.

- Cheng, S.-J. Tang, F. Komori, K. Kobayashi, T.-C. Chiang, and I. Matsuda, Proving Nontrivial Topology of Pure Bismuth by Quantum Confinement, *Phys. Rev. Lett.* **117**, 236402 (2016).
- [12] Y. Zhang, K. He, C. Z. Chang, C. L. Song, L. L. Wang, X. Chen, J. F. Jia, Z. Fang, X. Dai, W. Y. Shan, S. Q. Shen, Q. Niu, X. L. Qi, S. C. Zhang, X. C. Ma, and Q. K. Xue, Crossover of the three-dimensional topological insulator Bi_2Se_3 to the two-dimensional limit, *Nat. Phys.* **6**, 584 (2010).
- [13] S. Jang, J. D. Denlinger, J. W. Allen, V. S. Zapf, M. B. Maple, J. N. Kim, B. G. Jang, and J. H. Shim, Evolution of the Kondo lattice electronic structure above the transport coherence temperature, [arXiv:1704.08247](https://arxiv.org/abs/1704.08247).
- [14] C. Petrovic, P. G. Pagliuso, M. F. Hundley, R. Movshovich, J. L. Sarrao, J. D. Thompson, Z. Fisk, and P. Monthoux, Heavy-fermion superconductivity in CeCoIn_5 at 2.3 K, *J. Phys.: Condens. Matter* **13**, L337 (2001).
- [15] D. G. Mazzone, N. Gauthier, D. T. Maimone, R. Yadav, M. Bartkowiak, J. L. Gavilano, S. Raymond, V. Pomjakushin, N. Casati, Z. Revay, G. Lapertot, R. Sibille, and M. Kenzelmann, Evolution of Magnetic Order from the Localized to the Itinerant Limit, *Phys. Rev. Lett.* **123**, 097201 (2019).
- [16] N. D. Mathur, F. M. Grosche, S. R. Julian, I. R. Walker, D. M. Freye, R. K. W. Haselwimmer, and G. G. Lonzarich, Magnetically mediated superconductivity in heavy fermion compounds, *Nature (London)* **394**, 39 (1998).
- [17] P. Monthoux, D. Pines, and G. G. Lonzarich, Superconductivity without phonons, *Nature (London)* **450**, 1177 (2007).
- [18] R. Settai, H. Shishido, S. Ikeda, Y. Murakawa, M. Nakashima, D. Aoki, Y. Haga, H. Harima, and Y. Onuki, Quasi-two-dimensional Fermi surfaces and the de Haas-van Alphen oscillation in both the normal and superconducting mixed states of CeCoIn_5 , *J. Phys.: Condens. Matter* **13**, L627 (2001).
- [19] P. M. Oppeneer, S. Elgazzar, A. B. Shick, I. Opahle, J. Rusz, and R. Hayn, Fermi surface changes due to localized-delocalized f-state transitions in Ce-115 and Pu-115 compounds, *J. Magn. Magn. Mater.* **310**, 1684 (2007).
- [20] T. Nomoto and H. Ikeda, Fermi surface evolution and d -wave superconductivity in CeCoIn_5 : Analysis based on LDA + DMFT method, *Phys. Rev. B* **90**, 125147 (2014).
- [21] A. Koitzsch, S. V. Borisenko, D. Inosov, J. Geck, V. B. Zabolotnyy, H. Shiozawa, M. Knupfer, J. Fink, B. Büchner, E. D. Bauer, J. L. Sarrao, and R. Follath, Hybridization effects in CeCoIn_5 observed by angle-resolved photoemission, *Phys. Rev. B* **77**, 155128 (2008).
- [22] A. Koitzsch, I. Opahle, S. Elgazzar, S. V. Borisenko, J. Geck, V. B. Zabolotnyy, D. Inosov, H. Shiozawa, M. Richter, M. Knupfer, J. Fink, B. Büchner, E. D. Bauer, J. L. Sarrao, and R. Follath, Electronic structure of CeCoIn_5 from angle-resolved photoemission spectroscopy, *Phys. Rev. B* **79**, 075104 (2009).
- [23] X.-W. Jia, Y. Liu, L. Yu, J.-F. He, L. Zhao, W.-T. Zhang, H.-Y. Liu, G.-D. Liu, S.-L. He, J. Zhang, W. Lu, Y. Wu, X.-L. Dong, L.-L. Sun, G.-L. Wang, Y. Zhu, X.-Y. Wang, Q.-J. Peng, Z.-M. Wang, S.-J. Zhang *et al.*, Growth, Characterization and Fermi Surface of Heavy Fermion CeCoIn_5 Superconductor, *Chin. Phys. Lett.* **28**, 057401 (2011).
- [24] C. H. Booth, T. Durakiewicz, C. Capan, D. Hurt, A. D. Bianchi, J. J. Joyce, and Z. Fisk, Electronic structure and f-orbital occupancy in Yb-substituted CeCoIn_5 , *Phys. Rev. B* **83**, 235117 (2011).
- [25] L. Dudy, J. D. Denlinger, L. Shu, M. Janoschek, J. W. Allen, and M. B. Maple, Yb valence change in $\text{Ce}_{1-x}\text{Yb}_x\text{CoIn}_5$ from spectroscopy and bulk properties, *Phys. Rev. B* **88**, 165118 (2013).
- [26] A. Koitzsch, T. K. Kim, U. Treske, M. Knupfer, B. Büchner, M. Richter, I. Opahle, R. Follath, E. D. Bauer, and J. L. Sarrao, Band-dependent emergence of heavy quasiparticles in CeCoIn_5 , *Phys. Rev. B* **88**, 035124 (2013).
- [27] Q. Y. Chen, D. F. Xu, X. H. Niu, J. Jiang, R. Peng, H. C. Xu, C. H. P. Wen, Z. F. Ding, K. Huang, L. Shu, Y. J. Zhang, H. Lee, V. N. Strocov, M. Shi, F. Bisti, T. Schmitt, Y. B. Huang, P. Dudin, X. C. Lai, S. Kirchner, H. Q. Yuan, and D. L. Feng, Direct observation of how the heavy-fermion state develops in CeCoIn_5 , *Phys. Rev. B* **96**, 045107 (2017).
- [28] A. Polyakov, O. Ignatchik, B. Bergk, K. Götze, A. D. Bianchi, S. Blackburn, B. Prévost, G. Seyfarth, M. Côté, D. Hurt, C. Capan, Z. Fisk, R. G. Goodrich, I. Sheikin, M. Richter, and J. Wosnitza, Fermi-surface evolution in Yb-substituted CeCoIn_5 , *Phys. Rev. B* **85**, 245119 (2012).
- [29] J. Klotz, K. Götze, I. Sheikin, T. Förster, D. Graf, J.-H. Park, E. S. Choi, R. Hu, C. Petrovic, J. Wosnitza, and E. L. Green, Fermi surface reconstruction and dimensional topology change in Nd-doped CeCoIn_5 , *Phys. Rev. B* **98**, 081105(R) (2018).
- [30] V. N. Strocov, Intrinsic accuracy in 3-dimensional photoemission band mapping, *J. Electron. Spectrosc. Relat. Phenom.* **130**, 65 (2003).
- [31] P. Zhang, P. Richard, T. Qian, Y.-M. Xu, X. Dai, and H. Ding, A precise method for visualizing dispersive features in image plots, *Rev. Sci. Instrum.* **82**, 043712 (2011).
- [32] S. Doniach and M. Sunjic, Many-electron singularity in X-ray photoemission and X-ray line spectra from metals, *J. Phys. C: Solid State Phys.* **3**, 285 (1970).
- [33] P. S. Kirchmann, L. Rettig, X. Zubizarreta, V. M. Silkin, E. V. Chulkov, and U. Bovensiepen, Quasiparticle lifetimes in metallic quantum-well nanostructures, *Nat. Phys.* **6**, 782 (2010).
- [34] E. G. McRae, Electronic surface resonances of crystals, *Rev. Mod. Phys.* **51**, 541 (1979).
- [35] E. McRae and M. Kane, Calculations on the effect of the surface potential barrier in LEED, *Surf. Sci.* **108**, 435 (1981).
- [36] M. Milun, P. Pervan, and D. P. Woodruff, Quantum well structures in thin metal films: simple model physics in reality?, *Rep. Prog. Phys.* **65**, 99 (2002).
- [37] H. Pfau, H. Soifer, J. A. Sobota, A. Gauthier, C. R. Rotundu, J. C. Palmstrom, I. R. Fisher, G.-Y. Chen, H.-H. Wen, Z.-X. Shen, and P. S. Kirchmann, Low work function in the 122-family of iron-based superconductors, *Phys. Rev. Materials* **4**, 034801 (2020).
- [38] S. Elgazzar, I. Opahle, R. Hayn, and P. M. Oppeneer, Calculated de Haas-van Alphen quantities of CeMIn_5 ($M = \text{Co, Rh, and Ir}$) compounds, *Phys. Rev. B* **69**, 214510 (2004).
- [39] K. Kummer, S. Patil, A. Chikina, M. Güttler, M. Höppner, A. Generalov, S. Danzenbächer, S. Seiro, A. Hannaske, C. Krellner, Y. Kucherenko, M. Shi, M. Radovic, E. Rienks, G. Zwirner, K. Matho, J. W. Allen, C. Laubschat, C. Geibel, and D. V. Vyalikh, Temperature-Independent Fermi Surface in the Kondo Lattice YbRh_2Si_2 , *Phys. Rev. X* **5**, 011028 (2015).

- [40] D. Leuenberger, J. A. Sobota, S.-L. Yang, H. Pfau, D.-J. Kim, S.-K. Mo, Z. Fisk, P. S. Kirchmann, and Z.-X. Shen, De-hybridization of f and d states in the heavy-fermion system YbRh_2Si_2 , *Phys. Rev. B* **97**, 165108 (2018).
- [41] H. Kim, Y. Yoshida, C.-C. Lee, T.-R. Chang, H.-T. Jeng, H. Lin, Y. Haga, Z. Fisk, and Y. Hasegawa, Atomic-scale visualization of surface-assisted orbital order, *Sci. Adv.* **3**, eaa0362 (2017).
- [42] M. Haze, Y. Torii, R. Peters, S. Kasahara, Y. Kasahara, T. Shibauchi, T. Terashima, and Y. Matsuda, In Situ STM Observation of Nonmagnetic Impurity Effect in MBE-grown CeCoIn_5 Films, *J. Phys. Soc. Jpn.* **87**, 034702 (2018).
- [43] F. Bobaru and G. Zhang, Why do cracks branch? A peridynamic investigation of dynamic brittle fracture, *Int. J. Fract.* **196**, 59 (2015).
- [44] M. Marder, Cracks cleave crystals, *Europhys. Lett.* **66**, 364 (2004).
- [45] E. Herrera, V. Barrena, I. Guillamon, J. A. Galvis, W. J. Herrera, J. Castilla, D. Aoki, J. Flouquet, and H. Suderow, One-dimensional moire charge density wave in the hidden order state of URu_2Si_2 induced by fracture, [arXiv:2003.07881](https://arxiv.org/abs/2003.07881).
- [46] H. Shishido, T. Shibauchi, K. Yasu, T. Kato, H. Kontani, T. Terashima, and Y. Matsuda, Tuning the dimensionality of the heavy fermion compound CeIn_3 , *Science* **327**, 980 (2010).
- [47] Y. Mizukami, H. Shishido, T. Shibauchi, M. Shimozawa, S. Yasumoto, D. Watanabe, M. Yamashita, H. Ikeda, T. Terashima, H. Kontani, and Y. Matsuda, Extremely strong-coupling superconductivity in artificial two-dimensional Kondo lattices, *Nat. Phys.* **7**, 849 (2011).
- [48] M. Shimozawa, T. Watashige, S. Yasumoto, Y. Mizukami, M. Nakamura, H. Shishido, S. K. Goh, T. Terashima, T. Shibauchi, and Y. Matsuda, Strong suppression of superconductivity by divalent ytterbium Kondo holes in CeCoIn_5 , *Phys. Rev. B* **86**, 144526 (2012).
- [49] N. Gauthier, J. A. Sobota, M. Hashimoto, H. Pfau, D.-H. Lu, E. D. Bauer, F. Ronning, P. S. Kirchmann, and Z.-X. Shen, Data for “Quantum well states in fractured crystals of the heavy fermion material CeCoIn_5 ”, doi: <https://doi.org/10.25740/px092px3282>.